A robust fully Mixed Finite Element model for flow and transport in unsaturated fractured porous media

Anis A. Younes, Hussein Hoteit, Rainer Helmig, Marwan Fahs

A robust fully Mixed Finite Element model for flow and transport in unsaturated fractured porous media

Anis Younes[1], Hussein Hoteit[2], Rainer Helmig[3], Marwan Fahs[1]

[1]ITES, University of Strasbourg, CNRS, ENGEES, 67000, Strasbourg, France.

[2] Physical Science and Engineering Division, King Abdullah University of Science and Technology (KAUST), Thuwal, Saudi Arabia

[3] Institute for Modelling Hydraulic and Environmental Systems, University of Stuttgart, Pfaffenwaldring 61, 70569 Stuttgart, Germany

Submitted to Advances in Water Resources

Contact author: Marwan Fahs

E-mail: fahs@unistra.fr

Abstract

A fully mixed finite element (MFE) model is developed for nonlinear flow and transport in unsaturated fractured porous media with matrix-fracture and fracture-fracture fluid and mass exchanges. The model is based on the discrete fracture matrix (DFM) approach and assumes cross-flow equilibrium in the fractures. The MFE method is employed for the spatial discretization of both flow and transport on the 2D-matrix elements as well as on the 1D-fracture elements. An upwind scheme is employed to avoid unphysical oscillations in the case of advection dominant transport. The temporal discretization is performed using high-order time integration methods and efficient automatic time-stepping schemes via the MOL.

Two test problems dealing with flow and mass transport in saturated and unsaturated fractured porous media are simulated to show the validity of the new model by comparison against (*i*) a 1D-2D Comsol finite element model and (*ii*) a 2D-2D Discontinuous Galerkin (DG) model where both fractures and matrix continua are discretized with small 2D mesh elements. The robustness and efficiency of the developed 1D-2D MFE model are then investigated for a challenging problem dealing with infiltration of contaminated water into an initially dry soil involving a fracture network.

The new model yields stable results for advection-dominated and advection-dispersion transport configurations. Further, the results of the 1D-2D MFE model are in very good agreement with those of the 2D-2D DG model for both configurations. The simulation of infiltration of contaminated water into a dry fractured soil shows that the 1D-2D MFE model is within 15 times more efficient than the 2D-2D DG model, which confirms the high benefit of using robust and efficient DFM models for the simulation of flow and transport in fractured porous media.

Key words:

Fractured porous media, discrete fracture matrix approach, unsaturated flow, advection-dispersion equation, mixed finite element, upwind scheme.

1. Introduction

Flow and transport in fractured porous media are important in many applications such as water resource management (Wireman 2003, Kavouri *et al*., 2017), contaminant transport (Berkowitz, 2002; Brutz and Rajaram 2017, Klammler *et al.* 2016), nuclear waste management (Follin and Stigsson 2014, Mattila and Tammisto 2012) and oil and gas production (Li *et al*., 2015; Shen *et al.*, 2016).

The flow and transport processes in fractured porous media can be significantly affected by the characteristics of the fractures, such as location, size, orientation, and aperture. The fractures can be empty, or contain a filling material (Berre *et al*., 2019). In this work, the fractures are considered filled with a porous medium with different properties from the porous matrix, as in Khoobor *et al*. (2020). Two approaches are commonly used for modeling flow in fractured porous media (Berre *et al*., 2019). The first approach is based on an implicit representation of the fractures and includes both single-continuum and multi-continuum models. In single-continuum models, the fractures are taken into account by calculating an equivalent permeability of the porous medium, which depends on the properties of the fractures and the fracture network (Durlofsky, 1991; Liu *et al*., 2016). In multi-continuum models, the fractured porous medium is represented by two or more superimposed media with their own flow and/or transport equations. Among these, the well-known dual porosity model which considers superposition of a low permeability continuum representing the matrix with a high permeability continuum representing the fractures (Jourde *et al*., 2002; Kordilla *et al*., 2012). The two continua are then linked by a linear exchange term. More sophisticated multi-continuum models have been developed for aquifers with high heterogeneities, such as karst

aquifers, to include different levels of porosities and cavities (Kuhlman *et al*., 2015; Wu *et al*., 2004).

The second approach uses on an explicit representation of the fractures. Among this approach, the discrete fracture network (DFN) model. With DFN, the geometry and properties of discrete fractures are explicitly incorporated as a central component controlling flow and transport. Discrete fracture matrix (DFM) models consider that flow and transport processes occur through both, the porous matrix and the explicitly represented fractures. As a consequence, the DFM model is more appropriate for handling fractures in a permeable porous medium (Berre *et al*., 2019). Considering that the aperture of the fractures is small as compared to the matrix scale, the main idea of DFM is to use the cross-flow equilibrium concept across the fractures (Noorishad and Mehran, 1982; Baca *et al*., 1984; Granet *et al*., 1998; Hoteit *et al*.,2008). As a consequence, the fractures can be discretized with elements of co-dimension one with respect to the dimension of the surrounding matrix (Flemish *et al*., 2018; Martin *et al*., 2005), such as 1D fracture elements with 2D matrix elements. This simplification makes DFM models much more efficient than the single porosity 2D-2D model, where 2D elements are used for both matrix and fracture continua. Note that the applicability of the 2D-2D models is often hampered by their expansive computational cost since they require very fine mesh elements to correctly discretize the fractures with small apertures.

Hoteit and Firoozabadi (2005; 2006) employed DFM models assuming cross-flow equilibrium between the fractures and the adjacent matrix gridcells by imposing the pressure at a fracture and at the adjacent gridcells to be equal. Although efficient, this assumption still requires small mesh elements next to the fractures (Hoteit and Firoozabadi, 2008). To avoid this constraint, Hoteit and Firoozabadi (2008) proposed solving the flow equation with the hybrid formulation of the mixed finite element (MFE) method. This formulation has the

pressure at the gridcell interfaces as degrees of freedom (DOF), and hence, the cross-flow equilibrium can be directly assumed across the fractures (Hoteit and Firoozabadi, 2008). In this way, the matrix pressure at an element edge and the pressure at the fracture, which coincides with that edge, are assumed to be equal. As a consequence, no constraints are required for the mesh discretization near the fractures (Hoteit and Firoozabadi, 2008). This powerful feature is extended in this work by developing a fully MFE model for both unsaturated flow and transport in the porous matrix and in the fracture continuum.

The MFE (Raviart and Thomas, 1977; Chavent and Jaffré, 1986) is a robust numerical method for solving diffusion problems, which has recently received attention in geosciences. Indeed, with MFEs, the flux and the pressure unknowns are approximated simultaneously. The MFE method ensures local mass balance and can easily handle general unstructured meshes (Younes *et al*., 2010). Further, it yields an accurate velocity field in highly heterogeneous and anisotropic media (Durlofsky, 1994). The hybridization procedure of the MFE method allows improving its efficiency by reducing the total number of unknowns and producing a final system with a positive symmetric definite matrix (Chavent and Jaffré, 1986). The unknowns, in this case, are the traces of the variable at the edges.

A lumped formulation of the MFE method has been developed by Younes *et al*. (2006) to improve the monotonicity of the solution and reduce the unphysical oscillations observed with transient problems. Belfort *et al*. (2009) showed that the lumped formulation is more efficient and more robust than the standard one for the simulation of water infiltration into initially dry soils. Further, contrarily to the standard MFE method, the lumped formulation maintains the time derivative continuous and thus, allows employment of high-order time integration methods via the method of lines (MOL), which can be very efficient for solving nonlinear problems (Fahs *et al*., 2009 and Younes *et al*., 2009).

Although the MFE method is well adapted for diffusion type equations, when applied for the advection-dispersion transport equation, the solution can exhibit strong unphysical oscillations because of the hyperbolic nature of the advection operator. Therefore, the main objective of this work is to develop a stable MFE model for unsaturated flow and mass transport through both the 2D-matrix and the 1D-fracture elements. Both fluid and contaminant matrix-fracture and fracture-fracture exchanges are implicitly taken into account, without using any transfer functions, even for the case of several intersecting fractures. To avoid instabilities caused by the hyperbolic advection term, we use a robust monotonic upwind MFE scheme where the traces of concentration at edges are upwinded depending on the direction of the local velocity. An implicit scheme is used for the time discretization of the flow and transport equations. This alleviates restriction on the size of the time step from the CFL condition of explicit schemes. For the sake of brevity, the lumped hybrid MFE method employed in this work will also be denoted MFE.

Modeling flow and transport in unsaturated fractured porous media is likely to be highly CPU consuming due to (*i*) the strongly nonlinear Richards flow equation (RE), (*ii*) the high contrast of permeability between the conductive fractures and the low permeable matrix and (*iii*) the presence of sharp wetting and/or contaminant fronts. These difficulties make the commonly used, first-order backward Euler scheme combined with the heuristic time step management, inappropriate to obtain accurate solutions in a reasonable CPU time. To overcome these difficulties, time integration is performed using high-order time integration methods via the Method of Lines (MOL). The MOL allows versatile time step length and order of the temporal discretization to reduce the computational time while maintaining accuracy. The MOL was shown to be effective for the solution of the RE in the unsaturated zone (Fahs *et al*, 2009; Khoobor *et al*., 2020) and is used hereafter for the first time for coupled flow and transport through unsaturated fractured porous media.

This article is structured as follows. In section 2, we recall the nonlinear mathematical models governing flow and advection-dispersion transport processes in unsaturated porous media. In section 3, we develop a robust fully MFE formulation for the solution of flow and transport both in the porous matrix and in the fracture continuum. In section 4, numerical experiments are performed for flow and transport in saturated and unsaturated fractured porous media to investigate the validity and robustness of the new 1D-2D MFE model. Some conclusions are given in the last section of the article.

2. Governing Equations

The porous matrix is assumed permeable, and the fractures are infilled by a porous medium whose physical characteristics are different from those of the porous matrix. Flow in variably saturated porous media, both in the matrix and through the fractures, is assumed to be ruled by the mass conservation of the fluid:

$$\frac{\partial \theta}{\partial t} = \left(c(h) + S_S \frac{\theta}{\theta_S} \right) \frac{\partial H}{\partial t} = -\nabla \cdot \boldsymbol{q} = 0 \tag{1}$$

and the Darcy-Buckingham law:

$$\boldsymbol{q} = -k_r \boldsymbol{K} \nabla H \tag{2}$$

where $c(h) = \partial\theta/\partial h$ is the specific moisture capacity [L^{-1}], S_S is the specific mass storativity related to head changes [L^{-1}], θ is the current water content [L^3L^{-3}], θ_S is the saturated water content [L^3L^{-3}], $H = h + y$ is the freshwater head [L], h is the pressure head [L], y is the upward vertical coordinate [L], t is the time [T], $\boldsymbol{q}$ is the Darcy velocity [LT^{-1}], k_r is the relative conductivity [-], $\boldsymbol{K} = \frac{\rho g}{\mu}\boldsymbol{k}$ is the hydraulic conductivity tensor [LT^{-1}], ρ is the fluid

density [ML^{-3}], g is the gravity acceleration [LT^{-2}], μ is the fluid dynamic viscosity [$ML^{-1}T^{-1}$] and $\boldsymbol{k}$ is the permeability of the rock matrix as a tensor, or that of the fracture, as a scalar [L^2].

The transport of contaminants in the unsaturated porous matrix and through the unsaturated fractures is ruled by the advection-dispersion equation:

$$\frac{\partial(\theta C)}{\partial t} + \nabla.(\boldsymbol{q}C) - \nabla.(\boldsymbol{D}\nabla C) = 0 \tag{3}$$

where C [-] is the relative concentration [-] and $\boldsymbol{D}$ is the dispersion tensor given by:

$$\boldsymbol{D} = D_m \boldsymbol{I} + (\alpha_L - \alpha_T)\boldsymbol{q} \otimes \boldsymbol{q} / |\boldsymbol{q}| + \alpha_T |\boldsymbol{q}| \boldsymbol{I} \tag{4}$$

In which α_L and α_T are the longitudinal and transverse dispersivities [L], D_m is the pore water diffusion coefficient [L^2T^{-1}] and $\boldsymbol{I}$ is the unit tensor.

The standard van Genuchten (van Genuchten, 1980) model is used for the relationship between water content and pressure head:

$$S_e = \frac{\theta(h) - \theta_r}{\theta_s - \theta_r} = \begin{cases} \dfrac{1}{\left(1 + |\alpha h|^n\right)^m} & h < 0 \\ 1 & h \geq 0 \end{cases} \tag{5}$$

where α [L^{-1}] and n [-] are the van Genuchten parameters, $m = 1 - 1/n$, S_e is the effective saturation [-], and θ_r is the residual water content [L^3L^{-3}].

The conductivity-saturation relationship is analytically expressed from the Mualem (Mualem, 1976) model,

198 $$k_r = S_e^{1/2}\left[1-\left(1-S_e^{1/m}\right)^m\right]^2 \quad (6)$$

199 The nonlinear system (1)-(6) is solved numerically on (*i*) unstructured triangular 2D elements
200 for the porous matrix and (*ii*) linear 1D elements for fracture branches. All hydraulic and
201 transport parameters in the system (1)-(6) are defined elementwise, and therefore, they can be
202 different for each matrix or fracture element.

203 ## 3. The fully MFE numerical model

204 In this session, we recall the main stages for developing a robust MFE formulation for the
205 solution of the flow and transport equations both in the porous matrix and in the fractures.

206 *3.1 Discretization of the flow equation in the porous matrix*

207 With the MFE method, the velocity $\boldsymbol{q}$ inside each triangular element E is approximated
208 using the linear Raviart-Thomas basis functions (see Figure 1):

209 $$\boldsymbol{q} = \sum_{j=1}^{3} Q_j^E \boldsymbol{w}_j^E \quad (7)$$

210 where Q_j^E is the flux across the edge ∂E_j of E and $\boldsymbol{w}_j^E = \frac{1}{2|E|}\begin{pmatrix} x-x_j^E \\ y-y_j^E \end{pmatrix}$ is the Raviart-
211 Thomas basis functions (Raviart and Thomas, 1977) with $\left(x_j^E, y_j^E\right)$ the coordinates of the
212 node j faced to the edge ∂E_j of E and $|E|$ the area of E.

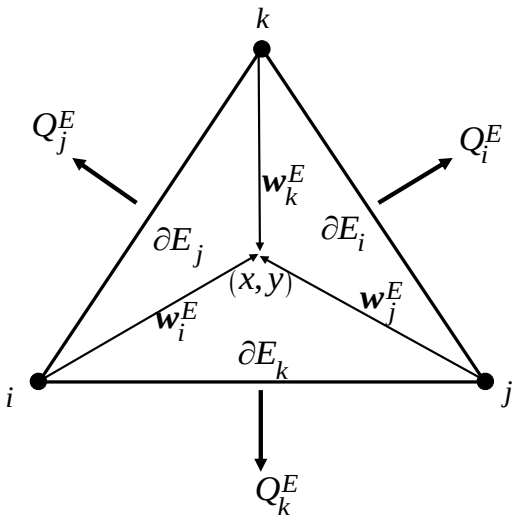

213

214 **Figure 1**: RT0 vectorial basis functions and orientation of fluxes for a 2D triangular element.

215 Using $\boldsymbol{w}_i^E$ as a test function, the variational formulation of the Darcy law Eq. (2) writes

216 $$\int_E \left(k_r^{-1}\boldsymbol{K}^{-1}\boldsymbol{q}\right).\boldsymbol{w}_i^E = -\int_E \nabla H.\boldsymbol{w}_i^E = \int_E H\nabla.\boldsymbol{w}_i^E - \sum_j \int_{\partial E_j} H\boldsymbol{w}_i^E.\boldsymbol{\eta}_j^E \quad (8)$$

217 where $\boldsymbol{\eta}_j^E$ is the outward unit normal vector to the edge E_j.

218 Defining $\boldsymbol{B}^E$ the elemental matrix of terms $B_{i,j}^E = \int_E \left(k_r^{-1,E}\boldsymbol{K}^{-1,E}\boldsymbol{w}_j^E\right).\boldsymbol{w}_i^E$, we obtain (see

219 Younes *et al*., 2004 for details)

220 $$\boldsymbol{B}^E = \frac{1}{48|E|}\begin{pmatrix} 3\ell_{ij}+3\ell_{ik}-\ell_{jk} & -3\ell_{ij}+\ell_{ik}+\ell_{jk} & \ell_{ij}-3\ell_{ik}+\ell_{jk} \\ -3\ell_{ij}+\ell_{ik}+\ell_{jk} & 3\ell_{ij}-\ell_{ik}+3\ell_{jk} & \ell_{ij}+\ell_{ik}-3\ell_{jk} \\ \ell_{ij}-3\ell_{ik}+\ell_{jk} & \ell_{ij}+\ell_{ik}-3\ell_{jk} & -\ell_{ij}+3\ell_{ik}+3\ell_{jk} \end{pmatrix} \quad (9)$$

221 with $\ell_{ij} = \mathbf{r}_{ij}^T\left(k_r^{-1,E}\boldsymbol{K}^{-1,E}\right)^{-1}\mathbf{r}_{ij}$ and $\mathbf{r}_{ij}$ is the edge vector from the node i to the node j.

222 Using Eq. (7) and properties of $\boldsymbol{w}_i^E$, the Darcy Eq. (8) becomes

$$\sum_j B_{i,j}^E Q_j^E = \frac{1}{|E|}\int_E H - \frac{1}{|\partial E_i|}\int_{\partial E_i} H = H_E - TH_i^E \tag{10}$$

where H_E is the mean head at the element E and TH_i^E is the mean head at the edge ∂E_i.

Inverting Eq. (10) provides the water flux Q_i^E across the edge ∂E_i as

$$Q_i^E = \delta_i^E H_E - \sum_j B_{i,j}^{-1,E} TH_j^E \tag{11}$$

where $\delta_i^E = \sum_j B_{i,j}^{-1,E}$.

The lumped formulation of MFE is then used in the following steps

- In a first step, integration of the mass conservation Eq. (1) over the element E, assuming a steady-state flow $\left(\partial\theta/\partial t = 0\right)$ and substituting Eq. (11), yields

$$H_E = \sum_i \frac{\delta_i^E}{\delta^E} TH_i^E \tag{12}$$

where $\delta^E = \sum_i \delta_i^E$

Hence, the steady-state flux $\underline{Q}_i^E$ across the edge ∂E_i writes

$$\underline{Q}_i^E = \sum_j \left(\frac{\delta_i^E \delta_j^E}{\delta^E} - B_{i,j}^{-1,E} \right) TH_j^E \tag{13}$$

- In a second step, a lumped region R_i is constructed around each edge ∂E_i by joining the two nodes of ∂E_i to the element centers $\boldsymbol{x}_E$ and $\boldsymbol{x}_{E'}$ of the elements E and E' sharing the edge i (Figure 2).

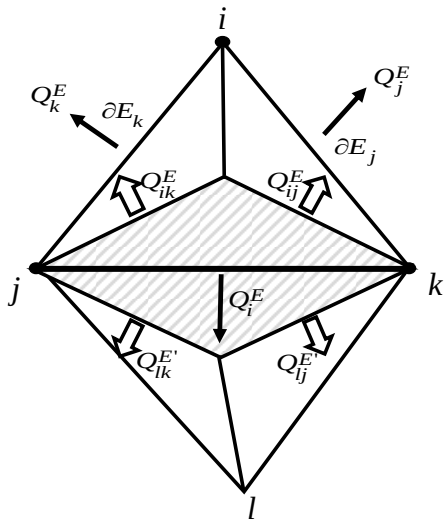

238

239 **Figure 2**: The lumping region R_i associated to the edge i sharing the elements E and E'

240 and formed by the two simplex regions S_i^E and $S_i^{E'}$.

241 The domain is now partitioned into lumping regions R_i (hatched area in Figure 2)
242 assigned to the edge *i* formed by the two simplex regions S_i^E and $S_i^{E'}$ for an inner
243 edge *i* and by the sole simplex region S_i^E for a boundary edge. The simplex region S_i^E
244 is defined by joining the centre of *E* with the nodes *j* and *k* forming the edge *i*. The
245 area of S_i^E is $\frac{|E|}{3}$.

246 • In a third step, the integration of the transient mass conservation Eq. (1) over the
247 lumped region R_i yields (see Figure 2 for notations):

248 $$\frac{|E|}{3} r_E \frac{dTH_i^E}{dt} + \frac{|E'|}{3} r_{E'} \frac{dTH_l^E}{dt} + \underline{Q}_{ij}^E + \underline{Q}_{ik}^E + \underline{Q}_{lj}^{E'} + \underline{Q}_{lk}^{E'} = 0 \qquad (14)$$

where $r_E = c(h_E) + S_S\,\theta(h_E)/\theta_S$ is the accumulation coefficient in Richards' equation and $\underline{Q}_{ij}^E$ the interior flux, evaluated using the RT0 approximation of the velocity inside the element E given by Eq. (7), which yields

$$\underline{Q}_{ij}^E = \frac{1}{3}\left(\underline{Q}_j^E - \underline{Q}_i^E\right) \tag{15}$$

Substituting Eq. (13) and Eq. (15) into Eq. (14), allows to write the mass conservation Eq. (14) over the lumping regions R_i assigned to the edge *i* as a continuity of fluxes between two adjacent elements E and E' sharing the edge *i* as follows

$$\begin{cases} Q_i^E + Q_i^{E'} = 0 \\ Q_i^E = \sum_j \left(\dfrac{\delta_i^E \delta_j^E}{\delta^E} - B_{i,j}^{-1,E} \right) TH_j^E - \dfrac{|E|}{3} r_E \dfrac{dTH_i^E}{dt} \end{cases} \tag{16}$$

The flow system is formed by Eq. (16) for all the mesh edges which do not coincide with a fracture and solved for the mean head at edges TH_i by imposing continuity of the head at the interface of the elements $\left(TH_i = TH_i^E = TH_i^{E'}\right)$. The obtained system is highly nonlinear since the local matrix $\boldsymbol{B}$, and the accumulation term r depend on the pressure head. In the case of a Dirichlet condition with a prescribed head H_{imp} at the boundary edge *i*, Eq. (16) is replaced by $TH_i = H_{imp}$. If the boundary edge *i* has a prescribed flux Q_{imp} (Neumann boundary condition), Eq. (16) becomes $Q_i^E + Q_{imp} = 0$.

Note that, contrarily to the standard MFE method, the time derivative remains continuous in Eq. (16), which facilitates employment of high-order methods for the time discretization.

3.2 Spatial discretization of the flow in the presence of a fracture

Let's consider a fracture k of length ℓ_k and aperture e_k. The fracture k coincides with the edge i shared by the adjacent matrix-elements E and E' (see Figure 3). The flow through the fracture occurs between it's two nodes of pressures NH_1^k and NH_2^k. The flux Q_i^E (respectively $Q_i^{E'}$) represents the matrix-fracture fluid exchange between E (respectively E') and the fracture k.

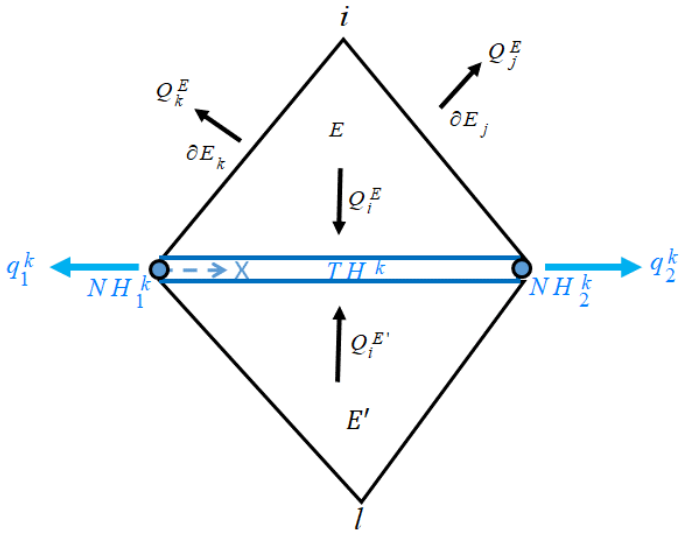

Figure 3: Schematic representation of the one-dimensional fracture k, which coincides with the edge i shared by the matrix elements E and E'. The flux Q_i^E (respectively $Q_i^{E'}$) represents the matrix-fracture fluid exchange between E (respectively E') and k.

The one-dimensional flow through the fracture k is discretized with the MFE method, which assumes a linear variation of the velocity q^k inside k,

$$q^k = q_1^k w_1^k + q_2^k w_2^k \tag{17}$$

with $q_{j=1,2}^k$ the flux leaving the node $j=1,2$ of the fracture k, $w_1^k = \dfrac{x-\ell_k}{e_k \ell_k}$ and $w_2^k = \dfrac{x}{e_k \ell_k}$ are the one-dimensional velocity interpolation functions using the local coordinate $x \in [0, \ell_k]$.

The mass conservation Eq. (1) integrated over the fracture k of length ℓ_k and aperture e_k yields

$$e_k \ell_k r_k \frac{dTH^k}{dt} + q_1^k + q_2^k - Q_i^E - Q_i^{E'} = 0 \tag{18}$$

with TH^k the mean head in the fracture *k* and $r_k = c(h_k) + S_S^k \frac{\theta_k}{\theta_S}$ the accumulation coefficient related to *k*, Q_i^E and $Q_i^{E'}$ are the water fluxes from the element *E* and *E*' representing matrix-fracture exchange.

The variational formulation of the Darcy law Eq. (2) on the fracture k writes

$$\sum_j q_j^k \int_0^{\ell_k} w_i^k w_j^k = -k_r^k \mathrm{K}_f^k \int_0^{\ell_k} (\nabla H) w_i^k \tag{19}$$

Integration by part leads to

$$\sum_j q_j^k \int_0^{\ell_k} w_i^k w_j^k = \frac{k_r^k \mathrm{K}_f^k}{e_k} \left(TH^k - NH_i^k \right) \tag{20}$$

where NH_i^k corresponds to the head at the node *i* located at the extremity of the fracture k.

Using numerical integration, based on the trapezoidal rule, for the calculation of the left term (see Koohbor *et al*., 2020) yields

$$q_i^k = e_k k_r^k \frac{2K_f^k}{\ell_k} \left(TH^k - NH_i^k \right) \tag{21}$$

296 The cross-flow equilibrium assumption is then employed by prescribing equality of the matrix
297 edge head and the fracture head $\left(TH_i^E = TH_i^{E'} = TH^k\right)$. Thus, substituting Eq. (21) and Eq.
298 (16) into Eq. (18) yields

$$\sum_j \left(\frac{\delta_i^E \delta_j^E}{\delta^E} - B_{i,j}^{-1,E} \right) TH_j^E + \sum_j \left(\frac{\delta_i^{E'} \delta_j^{E'}}{\delta^{E'}} - B_{i,j}^{-1,E'} \right) TH_j^{E'} - e_k k_r^k \frac{2K_f^k}{\ell_k} \left(2TH_i^E - NH_1^k - NH_2^k \right) - \left(\frac{|E|}{3} r_E + \frac{|E'|}{3} r_{E'} + e_k \ell_k r_k \right) \frac{dTH_i^E}{dt} = 0 \tag{22}$$

299

300 To close the system of Eq. (22), the mass conservation is written at each intersection of
301 fracture branches. At the node *i* shared by *k* fracture branches, we impose

$$\sum_k q_i^k = 0 \tag{23}$$

302

303 Using Eq. (21), we obtain

$$\sum_k e_k k_r^k \frac{2K_f^k}{\ell_k} \left(TH^k - NH_i^k \right) = 0 \tag{24}$$

304

305 Finally, the global flow system is formed by Eq. (16) for all the edges which do not coincide
306 with a fracture and by Eq. (22) else. This system is supplemented by Eq. (24) for all the nodes
307 of the fracture branches and assuming the continuity of the head $\left(NH_i = NH_i^k\right)$ at the node *i*,
308 intersection of *k* fracture branches. Therefore, the final flow system has the heads at the edges
309 of the mesh plus the heads at the nodes of the fracture branches as unknowns.

310 *3.3 Discretization of the advection-dispersion transport equation in the porous matrix*

311 The transport of contaminants in the unsaturated porous matrix described by Eq. (3) writes:

312 $$C\left(\frac{\partial\theta}{\partial t}+\nabla.\boldsymbol{q}\right)+\theta\frac{\partial C}{\partial t}+\boldsymbol{q}\nabla C-\nabla.\left(\boldsymbol{D}\nabla C\right)=0 \quad (25)$$

313 Using the fluid mass conservation Eq. (1), the transport equation can be written in the
314 following form:

315 $$\begin{cases}\theta\frac{\partial C}{\partial t}+\boldsymbol{q}\nabla C+\nabla.\tilde{\boldsymbol{q}}=0\\ \tilde{\boldsymbol{q}}=-\boldsymbol{D}\nabla C\end{cases} \quad (26)$$

316 The MFE method is now used for the spatial discretization of the transport equation. To this
317 aim, the dispersion vector $\tilde{\boldsymbol{q}}$ is approximated inside each triangular element E with the
318 Raviart Thomas vectorial basis functions as:

319 $$\tilde{\boldsymbol{q}}=\sum_j \tilde{Q}_j^E \boldsymbol{w}_j^E \quad (27)$$

320 where $\tilde{Q}_j^E=\int_{\partial E_j}\tilde{\boldsymbol{q}}_d.\boldsymbol{\eta}_j^E$ is the dispersive flux across the edge ∂E_j of the element E.

321 The variational formulation of Eq. (26) is written as

322 $$\int_E\left(\boldsymbol{D}_E^{-1}\tilde{\boldsymbol{q}}\right).\boldsymbol{w}_i^{\boldsymbol{E}}=-\int_E\nabla C.\boldsymbol{w}_i^{\boldsymbol{E}} \quad (28)$$

323 which can take the following form

324 $$\sum_j \tilde{B}_{i,j}^E\tilde{Q}_j^E=C_E-TC_i^E \quad (29)$$

325 where C_E is the mean concentration at the element E and TC_i^E is the trace of concentration
326 at the edge ∂E_i of the element E and $\tilde{\boldsymbol{B}}$ is the elemental matrix of terms
327 $\tilde{B}_{i,j}^E=\int_E\left(\boldsymbol{D}_E^{-1}\boldsymbol{w}_j^{\boldsymbol{E}}\right).\boldsymbol{w}_i^{\boldsymbol{E}}$

328 Inverting Eq. (29) yields the dispersive flux across ∂E_i as

329 $$\tilde{Q}_i^E = \sum_j \tilde{\boldsymbol{B}}_{i,j}^{-1,E} \left(C_E - TC_j^E \right) \tag{30}$$

330 An upwind lumped MFE scheme is used to avoid unphysical oscillations caused by the
331 hyperbolic advection part of the transport equation. The main steps of this scheme are as
332 follows:

333 • In a first step, both advective and transient terms are removed from the first equation
334 in the system of Eq. (26), yielding a steady-state dispersive flux $\underline{\tilde{Q}}_i^E$ expressed by
335 (similarly to Eq. (12)):

336 $$\underline{\tilde{Q}}_i^E = \sum_j \frac{\tilde{\delta}_i^E \tilde{\delta}_j^E}{\tilde{\delta}^E} TC_j^E - \sum_j \tilde{B}_{i,j}^{-1,E} TC_j^E \tag{31}$$

337 with $\tilde{\delta}_i^E = \sum_j \tilde{B}_{i,j}^{-1,E}$ and $\tilde{\delta}^E = \sum_i \tilde{\delta}_i^E$.

338 • In a second step, the integration of the advection-dispersion equation (26) over the
339 lumped region R_i writes (see Figure 2):

340 $$\left\{ \frac{|E|}{3} \theta_E \frac{\partial TC_i^E}{\partial t} + Q_{ij}^E TC_{ij}^E + Q_{ik}^E TC_{ik}^E - \left(Q_{ij}^E + Q_{ik}^E \right) TC_i^E - \underline{\tilde{Q}}_i^E \right\} + \{ \}' = 0 \tag{32}$$

341 where $Q_{ij}^E = \frac{1}{3}\left(Q_j^E - Q_i^E \right)$ is the interior flux between edges *i* and *j* (see Eq. (15)).

342 The interior concentration TC_{ij}^E is calculated using the upstream edge concentration
343 as:

344 $$TC_{ij}^{E} = \tau_{ij}^{E} TC_{i}^{E} + \left(1 - \tau_{ij}^{E}\right) TC_{j}^{E} \tag{33}$$

345 with $\tau_{ij}^{E} = 1$ for an outward flux $\left(Q_{ij}^{E} \geq 0\right)$, else $\tau_{ij}^{E} = 0$.

346 Thus, if we note Qt_{i}^{E} the total (advection + dispersion) flux leaving the element *E*
347 from the edge *i*, Eq. (32) can be rewritten as the continuity of the total flux between
348 two adjacent elements E and E' sharing the edge i as

349 $$\begin{cases} Qt_{i}^{E} + Qt_{i}^{E'} = 0 \\ Qt_{i}^{E} = \sum_{j} \left(\dfrac{\tilde{\delta}_{i}^{E} \tilde{\delta}_{j}^{E}}{\tilde{\delta}^{E}} - \tilde{B}_{i,j}^{-1,E} \right) TC_{j}^{E} + Q_{ij}^{E} \left(1 - \tau_{ij}^{E}\right)\left(TC_{i}^{E} - TC_{j}^{E}\right) + Q_{ik}^{E} \left(1 - \tau_{ik}^{E}\right)\left(TC_{i}^{E} - TC_{k}^{E}\right) - \theta_{E} \dfrac{|E|}{3} \dfrac{\partial TC_{i}^{E}}{\partial t} \end{cases}$$

350 (34)

351 *3.4 Spatial discretization of the advection-dispersion transport equation through a fracture*

352 Let's consider a fracture k of length ℓ_{k} and aperture e_{k} and x the local coordinate along k
353 with $x = 0$ at the first node of k and $x = \ell_{k}$ at the second node of k.

354 The diffusion coefficient D_{k} through the fracture *k* is approximated by

355 $$D_{k} = \alpha_{L}^{k} \left|\bar{q}_{k}\right| + D_{m}^{k} \tag{35}$$

356 where α_{L}^{k} is the longitudinal dispersivity through the fracture *k*, D_{m}^{k} is the molecular diffusion
357 through *k*, and $\bar{q}_{k} = \dfrac{\left(q_{2}^{k} - q_{1}^{k}\right)}{2e_{k}}$ is the mean velocity in the fracture *k*.

358 The dispersive flux $\tilde{\boldsymbol{q}} = -D\nabla C$ through the fracture is approximated using the MFE method.
359 Similarly to Eq. (21), the dispersive flux $\tilde{q}_{i}^{k}$ at the extremity $i = 1, 2$ of the fracture *k* writes

$$\tilde{q}_i^k = \frac{2e_k D_k}{\ell_k}\left(TC^k - N\tilde{C}_i\right) \tag{36}$$

where $N\tilde{C}_i$ is the concentration at the node *i*.

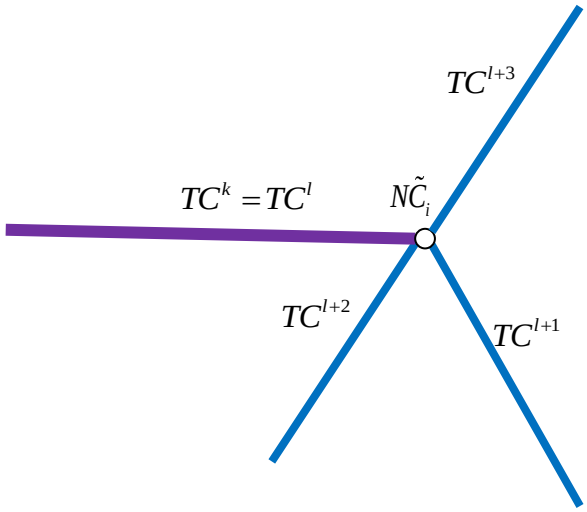

Figure 4: Intersection of multiple fracture branches.

Imposing the continuity of the dispersive fluxes arriving from all fracture branches sharing the node *i* (see Figure 4) writes

$$\sum_l \frac{2e_l D_l}{\ell_l}\left(TC^l - N\tilde{C}_j\right) = 0 \tag{37}$$

Which yields

$$N\tilde{C}_i = \frac{\sum_l \frac{e_l}{\ell_l} D_l TC^l}{\sum_l \frac{e_l}{\ell_l} D_l} \tag{38}$$

Substituting Eq. (38) into the flux Eq. (36) yields

375 $$\tilde{q}_i^k = \frac{2e_k D_k}{\ell_k}\left(TC^k - \frac{\sum_l \frac{e_l}{\ell_l} D_l TC^l}{\sum_l \frac{e_l}{\ell_l} D_l} \right) \quad (39)$$

376 The integration of the mass conservation equation over the fracture *k* which coincides with the
377 edge *i* shared by the two matrix elements *E* and *E'*, writes

378 $$\theta_k e_k \int_0^{\ell_k} \frac{\partial C}{\partial t} + e_k \int_0^{\ell_k} \nabla.(\boldsymbol{q}C) - e_k \int_0^{\ell_k} C\nabla.\boldsymbol{q} + e_k \int_0^{\ell_k} \nabla.\tilde{\boldsymbol{q}} - Qt_i^E - Qt_i^{E'} = 0 \quad (40)$$

379 The calculation of the different integrals yields

380 $$\theta_k e_k \ell_k \frac{\partial TC^k}{\partial t} + q_1^k C_1^{k,*} + q_2^k C_2^{k,*} - \left(q_1^k + q_2^k\right) TC^k + \tilde{q}_1^k + \tilde{q}_2^k = Qt_i^E + Qt_i^{E'} \quad (41)$$

381 where $C_i^{k,*}$ is the concentration at the node *i* of the fracture *k* given by

382 $$C_i^{k,*} = \lambda_i^k NC_{i,in}^k + \left(1 - \lambda_i^k\right)\overline{NC}_{i,out} \quad (42)$$

383 in which $NC_{i,in}^k = TC^k$ is the interior concentration and the parameter λ_i^k is used to select the
384 upstream concentration, it depends on the sign of q_i^k as

385 $$\lambda_i^k = \begin{cases} 1 & if \quad q_i^k \geq 0 \\ 0 & if \quad q_i^k < 0 \end{cases} \quad (43)$$

386 Hence, in the case of an outflow at the node *i* of *k*, the nodal concentration is $C_i^{k,*} = TC^k$,
387 whereas, in the case of an inflow at the node *i* of the fracture *k*, the nodal concentration is
388 $\overline{NC}_{i,out}$.

To calculate $\overline{NC}_{i,out}$, we use the contaminant conservation at the node *i*, shared by l fractures, which writes

$$\sum_{k=1}^{l} q_i^k C_i^{k,*} = 0 \tag{44}$$

Using Eq. (42) and Eq. (43), we obtain

$$\overline{NC}_{i,out} = \frac{\sum_{k=1}^{l} q_i^k \lambda_i^k TC^k}{\sum_{k=1}^{l} q_i^k \left(\lambda_i^k - 1\right)} \tag{45}$$

Note that the number of unknowns for the transport system to be solved does not depend on the number of fractures in the domain. Indeed, the final transport system has the concentration at edges as unknowns and is constructed as follows

- For all edges *i* sharing two matrix elements *E* and *E*' such that *i* does not coincide with a fracture *k*, Eq. (34) is solved for the unknown edge concentration TC_i assuming continuity of edge concentration $\left(TC_i = TC_i^E = TC_i^{E'}\right)$.

- For all edges *i* sharing two matrix elements *E* and *E*' such that *i* coincides with a fracture *k*, Eq. (41), in which we substitute Eq. (34), Eq. (39), Eq. (42), Eq. (43) and Eq. (45), is solved for the unknown edge concentration TC_i assuming that the concentration at the edge matrix and at the fracture are equal $\left(TC_i = TC_i^E = TC_i^{E'} = TC^k\right)$.

3.5 The temporal discretization of the nonlinear flow-transport system

The final nonlinear flow-transport system, formed by Eq. (16), Eq. (22), and Eq. (24) for the

flow and by Eq. (34) and Eq. (41) for the transport, is written in a single implicit system of ordinary differential equations (ODEs) of the general form

$$F\left(t,\boldsymbol{y},\boldsymbol{y}'\right)=0 \tag{46}$$

Where $\boldsymbol{y}=\left[\left(TH_i\right)_{i=1,..,nb\_edges},\left(NH_i\right)_{i=1,..,nb\_nodefractures},\left(TC_i\right)_{i=1,..,nb\_edges}\right]$ is the vector of unknowns formed by (*i*) the head traces at all the edges of the mesh (except boundary edges with prescribed head), (*ii*) the head at all the nodes corresponding to the extremity of fracture branches, and (*iii*) the concentration traces at all edges of the mesh (except boundary edges with prescribed concentration). Thus, the number of unknowns for the flow-transport system is approximately twice the number of edges plus the number of fractures.

For the time discretization, we use high-order methods, which are known to be more efficient and require less effort in the nonlinear solver compared to the lowest order methods (Farthing *et al.*, 2002). An efficient automatic time-stepping scheme is employed to improve the computational efficiency while maintaining accuracy (Tocci *et al.*, 1997; Kavetski *et al.*, 2001). The time integration is performed with the DASPK time solver, which uses the preconditioned Krylov iterative method to solve the linear systems arising at each time step. DASPK is based on the Fixed Leading Coefficient Backward Difference Formulas (FLCBDF), which has good stability properties and is well adapted for time integration of stiff problems (Kees and Miller, 2002). The nonlinear problem is linearized using the Newton method with a numerical approximation of the Jacobian matrix. To improve efficiency, the Jacobian is reused for several time steps and is calculated by the solver only when necessary. Furthermore, the column grouping technique (Hindmarsh, 1982) is employed to reduce the computational time for the evaluation of the Jacobian matrix by perturbing variables by group, knowing the structure and sparsity of the Jacobian.

During calculation, the order (up to fifth order) of the time discretization and the time step size are adapted to improve efficiency while the relative and absolute convergence criteria are maintained under a fixed tolerance (10^{-6} in this work).

4. Numerical experiments

In this section, three test problems dealing with flow and mass transport in saturated and unsaturated fractured porous media are simulated to investigate the robustness of the new MFE code. The first test case deals with flow and transport in a saturated porous medium involving a single fracture. This test case is used to validate the developed 1D-2D MFE code against the solution obtained with Comsol multiphysics 1D-2D model. Comosl uses the standard finite element (FE) method and an adaptive time stepping scheme. The test problem is also simulated with a 2D-2D model where 2D triangular elements are employed for the spatial discretization of both the matrix and the fractures continua using a very fine mesh in order to correctly discretize the fracture branches with a small aperture. We use the advanced 2D-2D DG model developed by Younes *et al*. (2021), based on the discontinuous Galerkin (DG) finite element and the multipoint flux approximation methods and high-order time integration techniques via the method of lines (MOL).

The second test case deals with flow and transport in a fractured unsaturated-saturated porous medium. The porous medium has initially wet conditions and involves a single fracture. This test case is used to validate the developed 1D-2D MFE model against the solution obtained with the 2D-2D DG model in the case of unsaturated flow.

The last test case is a challenging problem dealing with flow and transport into an initially dry soil containing a fracture network. This last problem is simulated to highlight the efficiency and robustness of the developed 1D-2D MFE model compared to the 2D-2D DG model.

4.1 Fractured saturated quarter-five-spot problem

We consider a quadratic 2D domain (quarter-five-spot configuration) of size $[0,1\text{m}]\times[0,1\text{m}]$ with impermeable walls except at the lower-left and the upper-right corners. The source at the lower-left corner is represented by a boundary flux $q_{inj}=10^{-3}\text{m/s}$ at $(0\le x\le 0.03\text{m})\cap(y=0)\cup(x=0)\cap(0\le y\le 0.03\text{m})$. The sink at the right-upper corner is represented by a Dirichlet boundary condition with a zero head at $(0.97\text{m}\le x\le 1\text{m})\cap(y=1)\cup(x=1)\cap(0.97\text{m}\le y\le 1\text{m})$. The porous medium is formed by a homogeneous material with a diagonal fracture of 1mm aperture, located between $(0.2\text{m},0.2\text{m})$ and $(0.8\text{m},0.8\text{m})$. The hydraulic and transport properties of the porous matrix and the fracture continuum are depicted in Table 1. The initial conditions correspond to a domain free from pollutants. The simulation is performed for a time of 3456s.

	K_s (m/s)	$S_s\ (1/m)$	θ_s	α_L (m)	α_T (m)	D_m (m^2/s)
Matrix	10^{-6}	10^{-10}	0.4	0.0	0.0	10^{-6}
Fracture	10^{-3}	10^{-10}	0.4	0.0	0.0	10^{-6}

Table 1: Hydraulic and transport parameters for the fractured saturated quarter-five-spot problem.

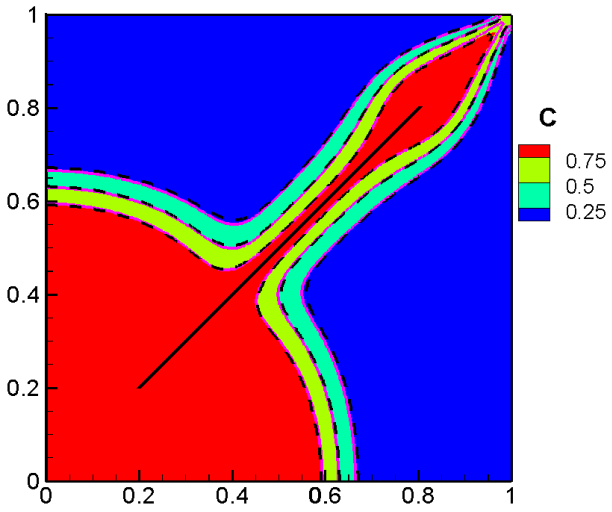

Figure 5: Concentration distribution for the fractured saturated quarter-five-spot problem. Results of the new 1D-2D MFE model (dashed lines), the 1D-2D Comsol FE model (purple lines), and 2D-2D DG model (color map).

The problem is simulated with the new 1D-2D MFE model as well as with the 1D-2D Comsol FE model and the 2D-2D DG model of Younes *et al.* (2021). In the latter, the hydraulic and transport parameters used for the fractures in the 1D-2D approach are attributed to the 2D triangular elements located inside the fractures. The 2D-2D DG model is used with a fine mesh with local mesh refinement around fractures. The three models were used with the MOL and a variable high-order (up to 5) time integration BDF method. Figure 5 shows that the three models yield almost similar concentration distributions, which demonstrates the validity of the developed 1D-2D MFE model for simulating flow and transport in fractured saturated porous media.

4.2 Infiltration of contaminated water in a fractured unsaturated-saturated porous medium.

This test case, inspired by the laboratory experiments of Vauclin *et al.*, (1979), was proposed by Koohbor *et al.* (2020) to investigate unsaturated flow in fractured porous media. The problem is extended hereafter to tackle both flow and transport in the case of a homogeneous porous medium, including a single inclined fracture. The domain has a rectangular shape of

300cm×200 cm with a water table located at 65cm from the bottom. Initial conditions correspond to a hydrostatic pressure distribution and a zero concentration in the domain. Boundary conditions are as follows: contaminated water is infiltrated under a constant flux of 335cm/day over the first 50cm of the soil surface. The lower 65cm of the right side of the domain has a Dirichlet boundary condition with a fixed head of 65cm. A no-flow boundary is prescribed for the rest of the boundaries. The homogeneous porous medium includes an inclined fracture of 1cm aperture and 2m length, located near the infiltration zone. The hydraulic and transport parameters are depicted in Table 2.

	K_s (m/s)	S_s (1/m)	θ_s	θ_r	α (1/m)	n	α_L (m)	α_T (m)	D_m (m^2/s)
Matrix	$5\ 10^{-5}$	10^{-10}	0.4	0.1	3.31	2.1	0	0	10^{-7}
Fracture	10^{-2}	10^{-10}	0.4	0.01	3.31	2.1	0	0	10^{-7}

Table 2: Hydraulic and transport parameters for the problem of infiltration of contaminated water into a fractured unsaturated-saturated porous medium.

The simulation of this problem cannot be performed with the 1D-2D Comsol FE model since Comsol cannot treat unsaturated flow in the fractures. The problem is simulated with the 1D-2D MFE model as well as with the 2D-2D DG model and the 2D-2D FE model of Comsol. Figure 6 depicts the water content and the concentration distributions at t = 1000s obtained with the three models. A good agreement is observed between the results of the three models for the volumetric water content as well as for the concentration contours (Figure 6).

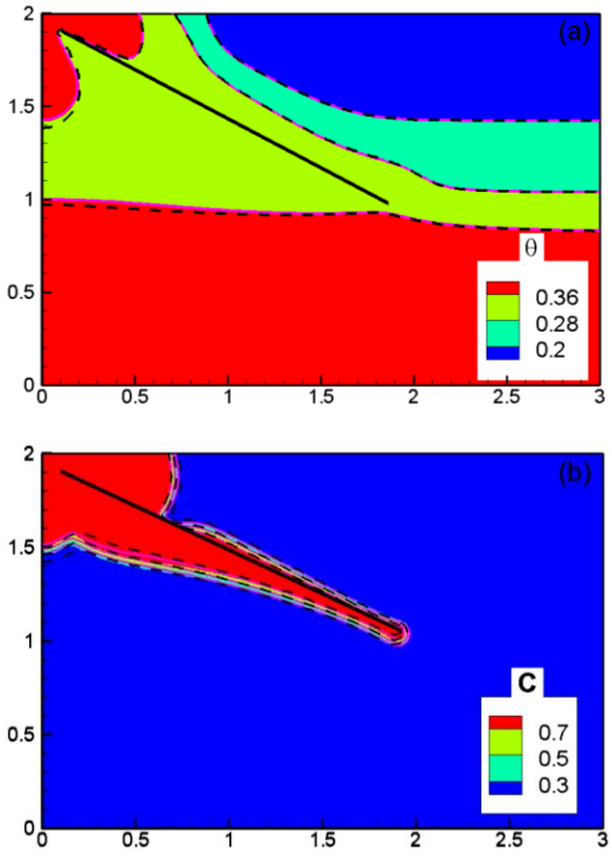

Figure 6: Water content (a) and concentration (b) distributions for the problem of infiltration of contaminated water in a fractured unsaturated-saturated porous medium. Results of the new 1D-2D MFE model (dashed lines), 2D-2D DG model (purple lines), and 2D-2D FE Comsol model (color map).

A more in-depth comparison is then performed between the new 1D-2D MFE model and the 2D-2D DG model. To this aim, the fluid and contaminant mass fluxes at the outlet are calculated with both models over the simulation time of 55 hours. The results of the Figure 7 show that the outlet fluid flux is almost constant after around 15 hours which indicates that an almost steady state water content distribution is reached at this time. A first contaminant front, caused by the fast mobility of the contaminated water through the fractures, is observed in the Figure 7 after around 10 hours. A second slower and more dispersed contaminant front was occurred, which was caused by the transport of the contaminant through the rock matrix. The

results of Fgure 7 show a very good agreement between the 1D-2D MFE and the 2D-2D DG models for both fluid and contaminant outlet mass fluxes. These results demonstrate the validity of the new 1D-2D MFE model for the simulation of flow and transport in fractured unsaturated porous media.

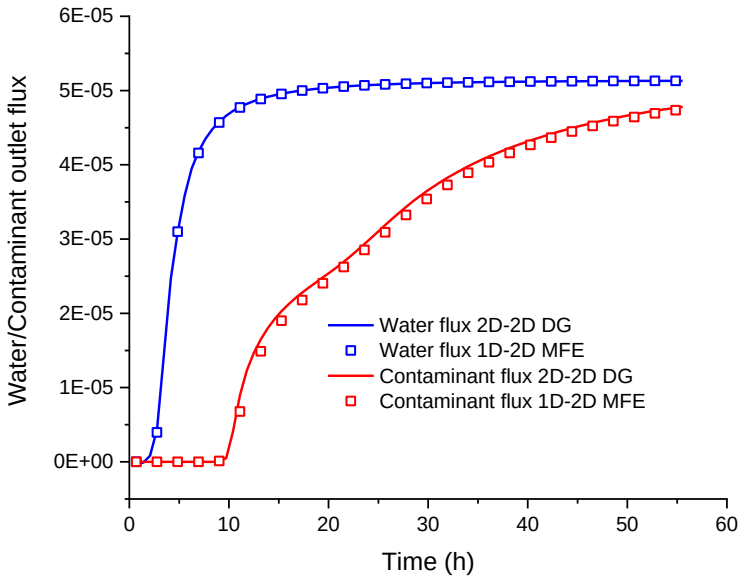

Figure 7: Outlet fluid and contaminant mass fluxes obtained with the 1D-2D MFE and the 2D-2D DG models for the problem of infiltration of contaminated water in a fractured unsaturated-saturated porous medium.

4.3 Infiltration of contaminated water in a fractured dry soil.

Simulation of the infiltration of contaminated water into initially dry soils is known to be challenging because of the presence of sharp wetting fronts (Zha *et al*., 2017). Sharp fronts are often the origin of unphysical oscillations, which can cause several convergence issues. To investigate the efficiency of the developed model for such situations, we simulate an infiltration problem, adapted from Koohbor *et al*. (2020). The fractured porous medium has a rectangular shape of 350cm in length and 200cm in height (Figure 8a). Left and right vertical boundaries are impermeable. A pressure head of -1000 cm is imposed at the bottom of the

538 domain. Water is injected at the right part of the surface ($300cm \le x \le 350cm$) with a constant
539 flow rate of 4×10^{-4} cm/s. The simulation is performed for a period of 2×10^{5}s. Clean water is
540 injected for the first half period $\left(C=0 \;\; if \;\; t \le 10^{5}s\right)$, and contaminated water is injected for
541 the second half period $\left(C=1 \;\; if \;\; t > 10^{5}s\right)$. Initial conditions correspond to a highly dry soil
542 with a head of -1000cm in both matrix and fracture continua. All fractures have an aperture of
543 1cm.

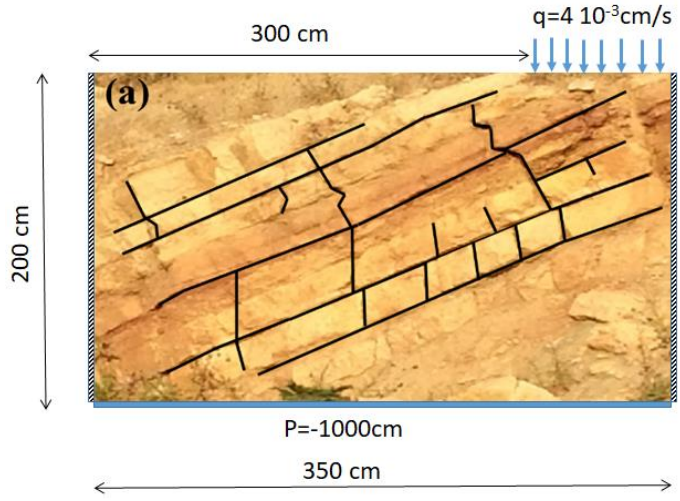

544

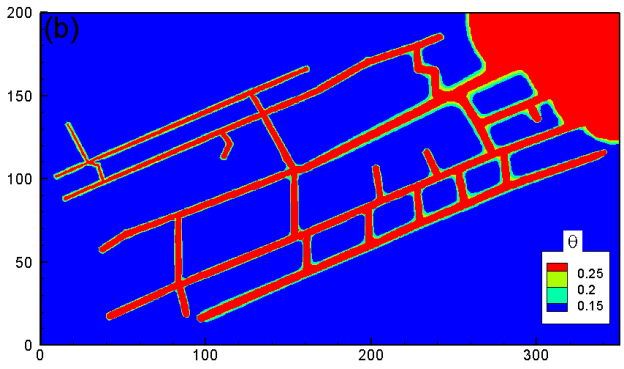

545

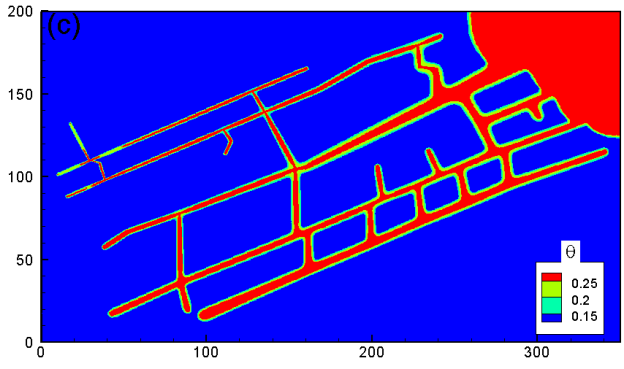

546

Figure 8: The problem of infiltration of contaminated water in a fractured initially dry soil: (a) domain and boundary conditions, (b) final water content distribution obtained with the 1D-2D MFE model and with the 2D-2D DG model (c).

The hydraulic parameters of the two continua are depicted in Table 3.

	K_s (cm/s)	S_s (1/cm)	θ_s	θ_r	α (1/cm)	n
Matrix	$5.25\ 10^{-6}$	10^{-8}	0.34	0.01	0.0139	1.6
Fracture	$1.16\ 10^{-2}$	10^{-8}	0.8	0.001	0.0139	1.6

Table 3: Hydraulic parameters for the problem of infiltration of contaminated water in a fracture initially dry soil.

The simulation of this last test case with the 2D-2D FE Comsol model encountered several convergence issues because of the initial high dry conditions. Indeed, the initial dry conditions are responsible of the appearance of several unphysical oscillations leading to the non-convergence of the nonlinear flow-transport model. These difficulties are avoided with the 2D-2D DG model thanks to the incorporated advanced numerical methods (see Younes et al. (2021) for more details). As a consequence, the results of the new 1D-2D MFE model are only compared to those of the 2D-2D DG model. The final water content distribution obtained with the two models is depicted in Figure 8. Similar distributions are obtained with the two models. As expected, the infiltrated water invades the fracture network, and high water saturation is observed in almost all fracture branches (Figure 8) because of their high saturated hydraulic conductivity, which is around 2200 times higher than that of the matrix continuum. Two configurations are investigated. The first configuration corresponds to a

566 highly advective transport problem. In this case, all dispersivities of the matrix and the
567 fractures are zero $\left(\alpha_L^m = \alpha_T^m = \alpha_L^f = 0\right)$, and a small molecular diffusion occurs in both
568 continua $\left(D_m^m = D_m^f = 10^{-6}\, cm^2/s\right)$. In the second configuration, a more significant dispersion
569 is considered for both continua with longitudinal and transverse dispersivities in the matrix,
570 respectively $\alpha_L^m = 5m$, and $\alpha_T^m = 2m$. The longitudinal dispersivity in the fractures is
571 $\alpha_L^f = 5m$. The molecular diffusion in both continua is $10^{-5}\, cm^2/s$. For the 1D-2D model, the
572 domain is discretized using 15400 triangles for the matrix continuum and 853 lines for the
573 fracture branches without any constraint on the size of mesh elements next to the fractures
574 (Figure 9a). The 2D-2D model is used on a fine mesh of 76000 elements with local mesh
575 refinement in the fractures in order to correctly discretize the flow and transport through the
576 fracture branches with a small aperture of 1cm (Figure 9b).

577

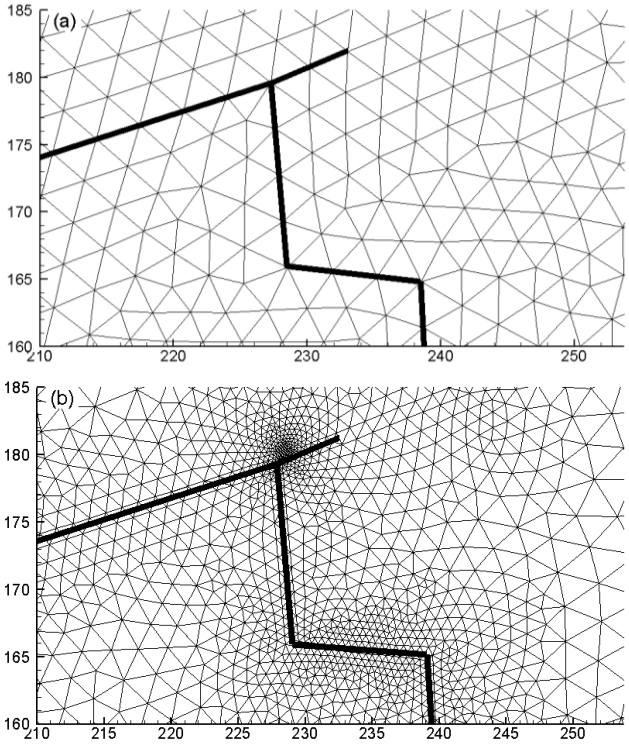

578

Figure 9: Spatial discretization for the 1D-2D MFE (a) model (fractures are represented by mesh edges) and for the 2D-2D DG (b) model (fractures are represented by small mesh elements).

Two versions of the 1D-2D MFE model are employed for the simulations: (*i*) the upwind scheme described above and (*ii*) a centered scheme where no upwinding is used for the advection operator in the matrix nor in the fractures. The results of Figure 10 show that the centered scheme provides similar results to the upwind scheme in the case of high dispersion (Figures 10d and 10e). However, in the case of advection-dominated transport, the centered scheme fails to provide accurate results and generates strong unphysical concentrations both in the matrix and in the fracture continuum (Figure 10b). The results of the upwind 1D-2D MFE model are exempted from unphysical oscillations (negative concentration are completely avoided) for both advection dominated and advection-dispersion configurations which demonstrates the robustness of the developed upwind 1D-2D MFE scheme. Furthermore, the solution of the upwind 1D-2D MFE model is in good agreement with the solution of the 2D-2D DG model both in the case of advection-dominated transport (Figure 10a vs 10c) and in the case of advection-dispersion transport (Figure 10d vs. 10f).

The advantage of using a high-order time discretization scheme is investgated by comparison against the first-order (conventional) scheme. The simulation using the upwind 1D-2D MFE model with a first-order time discretization scheme requires 20902 time steps and needs 6566s, whereas the high-order scheme requires only 3401 time steps and needs 375s. Thus, the high-order method is around four times faster than the first order method. Concerning the efficiency of the 1D-2D approach in comparison to the 2D-2D approach, the 2D-2D DG model required 5259s for the whole simulation, whereas the new 1D-2D MFE model requires only 375s. Thus, the new 1D-2D MFE model is around 15 times more efficient than the 2D-

603 2D DG model, which highlights the great benefit of robust and accurate 1D-2D models to
604 simulate flow and transport processes in unsaturated and saturated fractured porous media.
605

606

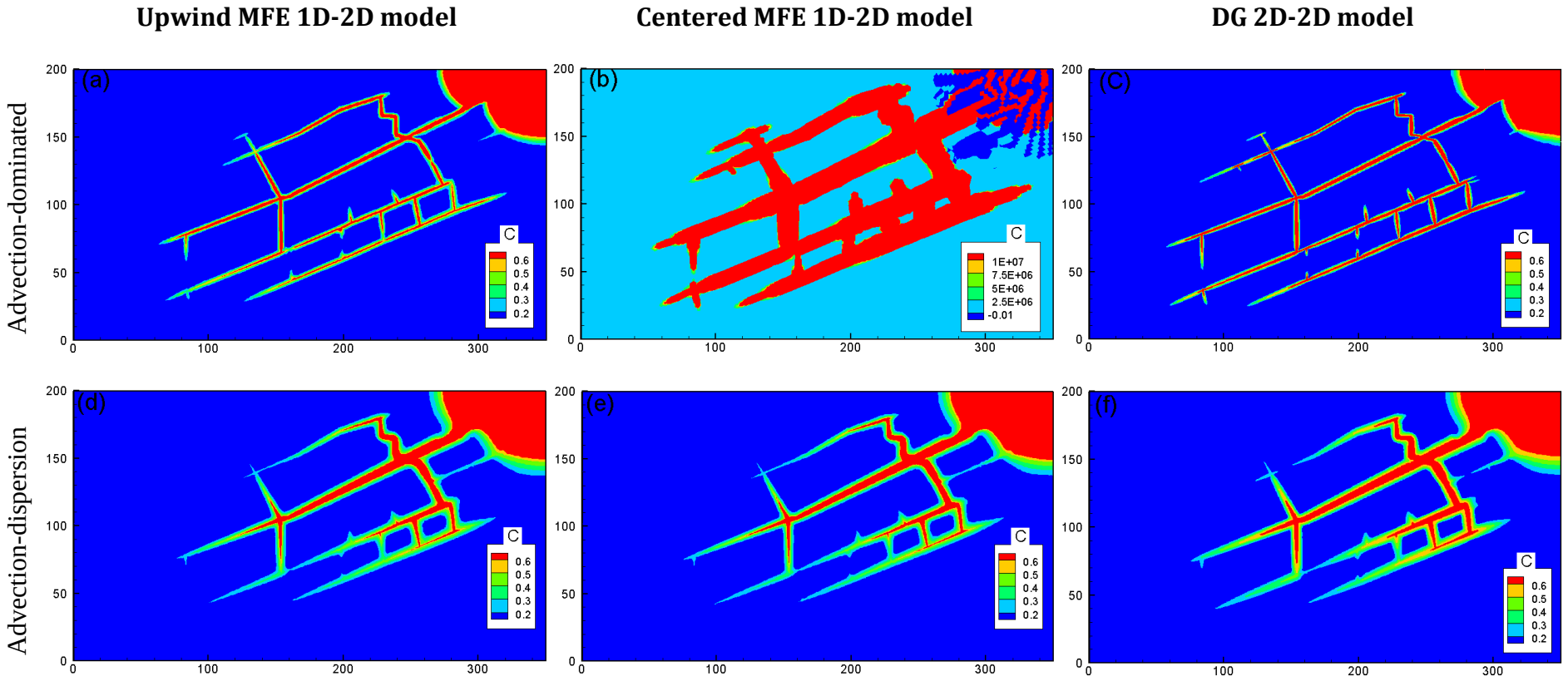

607 **Figure 10**: Infiltration of contaminated water in a fractured initially dry soil: Results of the upwind 1D-2D MFE model, the centered 1D-2D

608 MFE model and the 2D-2D DG model in the case of advection dominated transport $\left(\alpha_L^m = \alpha_T^m = \alpha_L^f = 0 \text{ and } D_m^m = D_m^f = 10^{-6}\, cm^2/s\right)$ and in the

609 case of advection-dispersion transport $\left(\alpha_L^m = \alpha_L^f = 5m,\ \alpha_T^m = 2m, \text{ and } D_m^m = D_m^f = 10^{-5}\, cm^2/s\right)$.

5. Conclusion

A new model has been developed for nonlinear flow and transport in unsaturated fractured porous media with implicit matrix-fracture and fracture-fracture fluid and contaminant exchanges. The model is based on the DFM approach, which describes fractures and matrix explicitly. Cross-flow equilibrium is assumed only across the fractures thanks to the MFE method which has been employed for the full spatial discretization of the flow and transport in both the matrix and the fracture continua. The MFE method avoids the constraints on the mesh size next to the fractures and allows to approximate the matrix-fracture and fracture-fracture exchange without any transfer functions. An upwind scheme is employed to avoid unphysical oscillations in the case of advection dominant transport. The time integration is performed with variable high-order methods via the MOL. An efficient automatic time-stepping scheme is used to improve the computational efficiency while maintaining accuracy of the nonlinear solver.

Three test problems dealing with flow and mass transport in saturated and unsaturated fractured porous media have been simulated to investigate the validity and robustness of the new 1D-2D MFE model. The first test case deals with the fractured quarter-five-spot problem and concerns flow and transport in a saturated porous medium involving a single fracture. The results of this test case with the 1D-2D MFE model were similar to those of the 1D-2D FE Comsol model and that of the 2D-2D DG model, which demonstrates the validity of the new model to simulate flow and transport in fractured saturated porous media.

The second test case deals with flow and transport in an unsaturated-saturated porous medium, including a single inclined fracture. This test case has been simulated with the 1D-2D MFE model as well as with the 2D-2D DG model and the 2D-2D FE model of Comsol

since the 1D-2D FE model of Comsol cannot treat unsaturated flow in fractures. A very good agreement is obtained between the three models for both the volumetric water content and the concentration contours, which demonstrates the validity of the new model for unsaturated fractured porous media.

The last test case is a challenging problem dealing with flow and transport in an initially dry soil containing a fracture network. For this problem, the 2D-2D FE Comsol model encountered several convergence issues because of the initial high dry soil conditions. The problem has been simulated using the 1D-2D MFE model using upwind and centered schemes. The results show that both schemes yield accurate results in the case of high dispersion. However, in the case of advection-dominated transport, only the upwind scheme provides stable results. The solution of the upwind 1D-2D MFE model is in good agreement with the solution of the 2D-2D DG model both in the case of advection-dominated transport and in the case of advection-dispersion transport.

The new 1D-2D MFE model is much more efficient than the 2D-2D DG model. The new model allows a speedup of around 15, which confirms the usefulness of efficient and accurate models based on the DFM approach for the simulation of flow and transport in fractured porous media.

REFERENCES

Wireman, M., 2003. EPA update: Characterization and management of ground water resources in fractured-rock hydrogeologic settings. Ground Water Monitoring & Remediation, 23(3), 34-40. doi:10.1111/j.1745-6592.2003.tb00681.x.

Kavouri, K.P., Karatzas, G.P., Plagnes, V., 2017. A coupled groundwater-flow-modelling and vulnerability-mapping methodology for karstic terrain management. Hydrogeol J 25, 1301–1317. https://doi.org/10.1007/s10040-017-1548-6

Berkowitz, B. 2002. Characterizing flow and transport in fractured geological media: a review. Advances in Water Resources, 25(8), 861–884. doi:10.1016/S0309-1708(02)00042-8.

Brutz, M., and Rajaram, H., 2017. Coarse-scale particle tracking approaches for contaminant transport in fractured rock. Applied Mathematical Modelling, 41, 549-561. doi: 10.1016/j.apm.2016.09.023.

Klammler, H., Hatfield, K., Newman, M. A., Cho, J., Annable, M. D., Parker, B. L., Cherry, J. A., and Perminova, I., 2016. A new device for characterizing fracture networks and measuring groundwater and contaminant fluxes in fractured rock aquifers. Water Resources Research, 52(7), 5400-5420. doi: 10.1002/2015WR018389.

Follin, S., and Stigsson, M., 2014. A transmissivity model for deformation zones in fracture crystalline rock and its possible correlation to in situ stress at the proposed high-level nuclear waste repository site at Forsmark, Sweden. Hydrogeology Journal, 22(2), 299-311. doi:10.1007/s10040-013-1078-9.

Mattila, J., and Tammisto, E., 2012. Stress-controlled fluid flow in fractures at the site of a potential nuclear waste repository, Finland. Geology, 40(4), 299-302. doi: 10.1130/G32832.1.

Li, X., Zhang, D., Li, S., 2015. A multi-continuum multiple flow mechanism simulator for unconventional oil and gas recovery. Journal of Natural Gas Science and Engineering 26, 652–669. https://doi.org/10.1016/j.jngse.2015.07.005

Shen, W., Xu, Y., Li, X., Huang, W., Gu, J., 2016. Numerical simulation of gas and water flow mechanism in hydraulically fractured shale gas reservoirs. Journal of Natural Gas Science and Engineering 35, 726–735. https://doi.org/10.1016/j.jngse.2016.08.078

Berre, I., Doster, F. & Keilegavlen, E. Flow in Fractured Porous Media: A Review of Conceptual Models and Discretization Approaches. Transp Porous Med 130, 215–236 (2019). https://doi.org/10.1007/s11242-018-1171-6

Koohbor, B.; Fahs, M.; Hoteit, H.; Doummar, J.; Younes, A.; Belfort, B. An Advanced Discrete Fracture Model for Variably Saturated Flow in Fractured Porous Media. Adv. Water Resour. 2020, 140, 103602

Durlofsky, L.: Numerical calculation of equivalent grid block permeability tensors for heterogenous porous media. Water Resour. Res. 27(5), 699–708 (1991)

Liu, R., Li, B., Jiang, Y., Huang, N.: Review:Mathematical expressions for estimating equivalent permeability of rock fracture networks. Hydrogeol. J. 24(7), 1623–1649 (2016)

Jourde, H., Cornaton, F., Pistre, S., Bidaux, P., 2002. Flow behavior in a dual fracture network. Journal of Hydrology 266, 99–119. https://doi.org/10.1016/S0022-1694(02)00120-8

Kordilla, J., Sauter, M., Reimann, T., Geyer, T., 2012. Simulation of saturated and unsaturated flow in karst systems at catchment scale using a double continuum approach. Hydrol. Earth Syst. Sci. 16, 3909–3923. https://doi.org/10.5194/hess-16-3909-2012

Kuhlman, K.L., Malama, B., Heath, J.E., 2015. Multiporosity flow in fractured low-

permeability rocks. Water Resources Research 51, 848–860. https://doi.org/10.1002/2014WR016502

Wu, Y.-S., Liu, H.H., Bodvarsson, G.S., 2004. A triple-continuum approach for modeling flow and transport processes in fractured rock. Journal of Contaminant Hydrology 73, 145–179. https://doi.org/10.1016/j.jconhyd.2004.01.002

Noorishad, J., and M. Mehran (1982), An upstream finite element method for solution of transient transport equation in fractured porous media, Water Resour. Res., 18(3), 588 – 596.

Baca, R., R. Arnett, and D. Langford (1984), Modeling fluid flow in frac tured porous rock masses by finite element techniques, Int. J. Numer. Methods Fluids, 4, 337 – 348.

Granet S, Fabrie P, Lemmonier P, Quitard M. A single phase flow simulation of fractured reservoir using a discrete representation of fractures. In: Proceedings of the 6th European conference on the mathematics of oil recovery (ECMOR VI), September 8–11, Peebles, Scotland, UK; 1998.

Hoteit H., Firoozabadi A. (2008) An efficient numerical model for incompressible two-phase flow in fractured media, Adv. Water Resour. 31, 891–905.

Flemisch B, Inga Berre, Wietse Boon, Alessio Fumagalli, Nicolas Schwenck, Anna Scotti, Ivar Stefansson, Alexandru Tatomir, Benchmarks for single-phase flow in fractured porous media, Advances in Water Resources, Volume 111, 2018, Pages 239-258, ISSN 0309-1708, https://doi.org/10.1016/j.advwatres.2017.10.036.

Martin, V., Jaffré, J., Roberts, J.E., 2005. Modeling fractures and barriers as interfaces for flow in porous media. SIAM J. Sci. Comput. 26 (5), 1667–1691.

Hoteit H, Firoozabadi A. Multicomponent fluid flow by discontinuous Galerkin and mixed methods in unfractured and fractured media. Water Resour Res 2005;41(11):W11412.

Hoteit H, Firoozabadi A. Compositional modeling of discrete-fractured media without transfer functions by the discontinuous Galerkin and mixed methods. SPE J 2006;11(3):341–52.

Raviart PA, Thomas JM. A mixed finite element method for second order elliptic problems, in Mathematical Aspects of Finite Element Method, Lecture Notes in Mathematics, 1977; Vol. 606, Springer, New York, 292-315.

Chavent G, J. Jaffré (1986), Mathematical models and finite elements for reservoir simulation, North-Holland, Amsterdam.

Younes, A., Ackerer, P., Delay, F. 2010. Mixed finite element for solving 2D diffusion-type equations. Reviews of Geophysics, 48(1).

Durlofsky, L. (1994), Accuracy of mixed and control volume finite element approximations to darcy velocity and related quantities, Water Resour. Res., 30(4), 965 – 974.

Younes, A., Ackerer, P., Lehmann, F., 2006. A new mass lumping scheme for the mixed hybrid finite element method. International Journal for Numerical Methods in Engineering 67(1), 89-107.

Belfort, B., Ramasomanan, F., Younes, A., Lehmann, F., 2009. An efficient Lumped Mixed Hybrid Finite Element Formulation for variably saturated groundwater flow. Vadose Zone Journal. 8, 352-362.

Fahs, M., Younes, A., Lehmann, F., 2009. An easy and efficient combination of the Mixed Finite Element Method and the Method of Lines for the resolution of Richards' Equation. Environmental Modelling & Software 24(9), 1122-1126.

Younes, A., Fahs, M., Ahmed, S., 2009. Solving density driven flow problems with efficient spatial discretizations and higher-order time integration methods. Advances in Water Resources 32(3), 340-352.

Fahs, M., Younes, A., Lehmann, F., 2009. An easy and efficient combination of the Mixed Finite Element Method and the Method of Lines for the resolution of Richards' Equation. Environmental Modelling & Software 24(9), 1122-1126.

van Genuchten, M.Th., 1980. A Closed-form Equation for Predicting the Hydraulic Conductivity of Unsaturated Soils. Soil Science Society of America Journal 44(5), 892-898.

Mualem, Y., 1976. A new model for predicting the hydraulic conductivity of unsaturated porous media. Water Resources Research 12, 513–522.

Younes, A., Ackerer, P., Chavent, G., 2004. From mixed finite elements to finite volumes for elliptic PDE in 2 and 3 dimensions. International Journal for Numerical Methods in Engineering, 59, 365–388.

Farthing, M.W., Kees, C.E., Miller, C.T., 2002. Mixed finite element methods and higher-order temporal approximations. Advances in Water Resources 25, 85-101.

Tocci, M.D., Kelly, C.T., Miller, C.T., 1997. Accurate and economical solution of the pressure-head form of Richards' equation by the method of lines. Advances in Water Resources 20, 1–14.

Kavetski, D., Binning, P., Sloan, S.W., 2001. Adaptative backward Euler time stepping with truncation error control for numerical modelling of unsaturated fluid flow. International Journal for Numerical Methods in Engineering 53,1301–1322.

Kees, C.E., Miller, C.T., 2002. Higher order time integration methods for two-phase flow. Advances in Water Resources 25(2), 159-177.

Hindmarsh, A.C., 1982. Large ordinary differential equation systems and software. IEEE Control System Magazine 2, 24-30.

Younes, A., Koohbor, B., Belfort, B., Ackerer, P., Doummar, J., Fahs, M., 2021. Modeling variable-density flow in saturated-unsaturated porous media: An advanced numerical model. Advances in Water Resources, Volume 159, January 2022, 104077. 10.1016/j.advwatres.2021.104077

Vauclin, M., Khanji, D., Vachaud, G., 1979. Experimental and numerical study of a transient, two-dimensional unsaturated-saturated water table recharge problem. Water Resour. Res. 15, 1089–1101. https://doi.org/10.1029/WR015i005p01089

Zha, Y., Yang, J., Yin, L., Zhang, Y., Zeng, W., Shi, L., 2017. A modified Picard iteration scheme for overcoming numerical difficulties of simulating infiltration into dry soil. Journal of Hydrology 551, 56–69.